Results in Engineering 27 (2025) 106149

Contents lists available at ScienceDirect

Results in Engineering

journal homepage: www.sciencedirect.com/journal/results-in-engineering

Research paper

Co-simulation model combining dynamic control and FEM for evaluation of PMSM drive cycle performance

Emil Lind *, Sandra Eriksson

Department of Electrical Engineering, Division of Electricity, Uppsala University, Lägerhyddsvägen 1, Uppsala, 752 37, Sweden

ARTICLE INFO

Keywords:
PMSM
Co-simulation
Efficiency
Pulse-width modulation
Drive cycle
Torque ripple
Harmonics
High-frequency effects

ABSTRACT

A novel co-simulation model, combining motor FEM simulations in Ansys Maxwell with an inverter and control system in Twin Builder and MATLAB/Simulink, is presented. The objective is to more closely resemble real-life motor performance and assess high-frequency effects and motor losses of different supply and control systems. The effects from a three-phase two-level inverter with pulse-width modulation for three different switching frequencies on motor losses, efficiency, and torque ripple have been evaluated. The results have been compared against an ideal sinusoidal current supply, ideal voltage supply and a built-in toolkit provided by Ansys Electronics. The WLTP drive cycle has been used, quantified using Energy Center of Gravity. The results show that a current source is insufficient to evaluate motor efficiency and torque ripple, with differences most visible at low energy operating points. With switching, the overall drive cycle efficiency differs by almost half a percent compared to a current source. While the switching frequency is high enough compared to the fundamental frequency, the differences in efficiency for varying switching frequencies are almost negligible. For high speeds, an efficiency increase can be seen when the switching frequency is lowered. The increase in losses due to current ripple is negated by a decrease in the average current magnitude.

1. Introduction

Approximately one third of the energy usage in the EU belongs to the transport sector, and it is also the main contributor to greenhouse gas emissions. New regulations, stricter CO_2 targets, and a rise in electric vehicles (EVs) have led to a decrease in emissions for newly registered cars [1], [2], although further reductions are necessary. Another important aspect is that most EVs today use permanent magnet synchronous motors (PMSMs), which contain rare-earth materials such as neodymium and dysprosium, and the mining and production of these materials have geopolitical and environmental implications. Because of this, many EV manufacturers are trying to find ways to limit the use of rare-earth materials, while still achieving high efficiency [3]. All of this increases the relevance for accuracy in machine performance, efficiency and emission estimation for real-life EV driving scenarios. One common way to represent these scenarios is using drive cycles, which can be used to estimate both losses and emissions [4]. In order to generate more precise CO_2 emission estimates and realistic driving scenarios, the Worldwide Harmonised Light Transport Vehicle Procedure (WLTP) was created [5], [6], and it replaced the New European driving cycle (NEDC) as the new standardized drive cycle in the EU. Several previous optimization studies have utilized different drive cycles [7], [8], [9].

A common way to evaluate motor performance is through finite element method (FEM). FEM allows for a deeper analysis of both transient and non-linear behavior, for example due to partial or complete saturation, something that is difficult to achieve for simplified models such as equivalent circuit models. FEM simulation for different operating points of a drive cycle can provide accurate estimations of energy use and losses. However, there are certain downsides to using FEM for complete drive cycles, namely that the process is resource-heavy and time-consuming for extensive time series. Previous studies have overcome this by using different quantification methods. By locating repeating values of torque and rotational speed in a drive cycle, the number of simulations can be minimized. Similar operating points can also be grouped together, further limiting the necessary computational effort. By reducing the resolution, that is, expanding the boundaries from which operating points are combined, the simulation time required for a complete drive cycle can be drastically reduced, although at the cost of accuracy. However, a study carried out previously by the authors evaluated the impact on overall drive cycle motor efficiency using quan-

* Corresponding author.
E-mail address: emil.lind@angstrom.uu.se (E. Lind).

https://doi.org/10.1016/j.rineng.2025.106149
Received 6 April 2025; Received in revised form 2 July 2025; Accepted 5 July 2025
Available online 15 July 2025

tification and found that the error was small even when the number of operating points was significantly reduced [10]. Another example is the Energy Centre of Gravity (ECG) [11]. This strategy minimizes the number of points by separating the operating range of the vehicle into a specified grid, finds the energy center for all operating points of each section, and only simulates using these energy center points. Depending on the amount of energy in each section, a weighted constant is assigned to each point, ensuring that sections with different energy levels represent an accurate part of the full drive cycle.

Pulse width modulation (PWM) switching introduces high-frequency current ripple. The ripple magnitude is caused by three different factors: switching frequency, machine inductance and DC-link voltage. However, the relationship between the fundamental electric frequency and the switching frequency, together with inductance and DC-link voltage, determines the ripple magnitude. DC-link voltage can be varied through the use of a DC/DC-converter, although it is often fixed [12]. Machine inductance can be changed with motor design, and switching frequency is governed by the control system and can be varied on demand. An increase in switching frequency results in lower inverter efficiency, while it could potentially increase motor efficiency.

The impact of current ripple and PWM switching on iron losses has been studied in multiple papers. In [13], the impact on iron losses for different switching frequencies is studied for frequencies ranging from 1 kHz to 20 kHz. This is also investigated in [14], although for switching frequencies between 10 kHz and 200 kHz. Similarly, impact on copper, iron and additional losses for an electric machine due to switching is investigated in [12], [15], [16].

Co-simulation models using Ansys Maxwell 2D, Twin Builder and Simulink have been constructed before [17], [18], [19], [20], [21]. [17] provides an overall description of how co-simulations can be performed, while [18] investigates how individual multi-slice 2D FEM simulations can be used to approximate motor skew. In [19], the authors describe some of the challenges using FEM co-simulations and also discuss methods of reducing computational effort, discussing both closed-loop control methods and using a semi-analytical motor model. In [21], the focus is on building and testing a model that combines space vector pulse width modulation (SVPWM) control with a PMSM, while in [20] the main objective is to analyze the transient behavior and the operating limits of an induction motor and detuning of the controller.

In [22], Ansys Maxwell 2D is used to extract an equivalent circuit model (ECM), which is then combined with a control model built using Simulink connected to an inverter constructed in Twin Builder. The co-simulation model is then used to evaluate high-frequency effects, losses, and dynamic performance. Similarly, in [23], a detailed methodology of how ECMs can be utilized in dynamic control simulations is described, which allows for quicker simulations while still accounting for the non-linear behavior of motors.

While these models account for non-linearity, they cannot achieve complete accuracy since full transient behavior is not accounted for.

In [24], another co-simulation model is developed, in which a strategy-circuit-field co-simulation methodology is used, investigating the impact and the mutual influence of motor, inverter, and control strategy. Both motor losses and inverter losses are calculated for set fundamental frequencies and loads.

In [25] a co-simulation model of a PMSM and direct torque control is created. The FEM software FLUX 2D is used to design the motor and is then combined with the control model in Matlab/Simulink, where a torque and speed response is analyzed.

None of these studies analyzes the efficiencies and torque ripple of multiple operating points for a specified drive cycle, or evaluates the effect of different control methods and switching frequencies.

This paper contributes to the field by combining FEM simulations with a dynamic motor control system, applying switched voltages and currents to the FEM software while having the system adjust itself based on motor operation. The study shows a comparison regarding efficiency and torque ripple between different operating modes and control methods, and showcases the importance of including switching effect analysis for motor efficiency studies. The study also explains how, by utilizing a quantification method together with good initialization parameters, it is possible to evaluate motor losses and torque ripple for a drive cycle, while still achieving the benefits of high-accuracy dynamic control.

In Section 1, a brief introduction to the study and area is described. Section 2 presents the previous theory. Section 3 describes the method used in this study, divided into four parts: Drive cycle description and quantification using ECG, machine description, co-simulation model explanation, and lastly, efficiency and loss calculations. Section 4 contains the results and discussion and Section 5 lists the most important conclusions.

2. Theory

2.1. Loss calculation

The calculation of iron losses has been the focus of many studies, and there are many different methods developed and used.

Iron loss calculation can be divided into two different categories: time domain and frequency domain.

A popular method to use when calculating iron losses for electric machines is the loss separation method [26]. Iron losses are divided into three parts: classical eddy current losses, P_c, hysteresis losses, P_h, and excess losses, P_e. The total iron losses can then be calculated with (1)-(4).

$$P_c = k_c (B_m f)^2 \tag{1}$$

$$P_h = k_h B_m^{\alpha} f \tag{2}$$

$$P_e = k_e B_m^{1.5} f^{1.5} \tag{3}$$

$$P_{ir} = P_c + P_h + P_e \tag{4}$$

where B_m is the peak magnetic flux density and P_{ir} is the volumetric iron losses. The value of α can range from 1.5-2.5. It is often assumed to be 2 given sinusoidal voltage supply [27].

Supplier material data, along with different curve fitting methods, can be used to find the coefficients. The eddy current coefficient can be calculated with (5).

$$k_c = \frac{\pi^2 d^2}{6\rho} \tag{5}$$

where d is the sheet thickness and ρ is the resistivity of the material.

By rearranging (4) and dividing by the frequency we get the expression shown in (6).

$$\frac{P_{ir} - \frac{\pi^2 d^2}{6\rho}(B_m f)^2}{f} = k_h B_m + k_e B^{1.5}\sqrt{f} \tag{6}$$

k_h is found when $f = 0$, and k_e can then be found through curve fitting.

In some models, these coefficients are considered constants, invariable to changes in induction and frequency. However, it is also possible to have floating coefficients, which work as functions of both induction and frequency.

Ansys Maxwell includes an extension, called "Machine toolkit", henceforth known as Ansys Machine Toolkit (AMT), which can be used to estimate the electromagnetic properties of a machine for full operation, including a torque/speed curve, losses and currents, among other things. This toolbox utilizes a method that combines a frequency domain-based iron loss with variable coefficients, see (7).

$$P_{ir} = \sum_{n=1}^{N} (k_h(B_n) n f B_n^2 + k_c(B_n, nf)(nf B_n)^2) \tag{7}$$

where k_h and k_c are functions and not constants. These are tabulated into a look-up table using material data and are then retrieved using cubic spline interpolation.

The previous method was based on the frequency domain. In Ansys Maxwell Transient Analysis, iron losses need to be calculated in the time domain, and (1)-(3) are modified into (8).

$$P_f = C_t |H_{irr}|^{y-x} |\frac{dB}{dt}|^x \tag{8}$$

where hysteresis loss is found when $x = 1$ and $y = 2$, classical eddy current loss when $x = y = 2$ and excess eddy current loss when $x = y = 1.5$. H_{irr} is the irreversible component of the magnetic field strength, $H_{irr} = H - H_{rev}$, with H_{rev} being the reversible part. H_{irr} is then found by approximating the area of the BH curve to that of an ellipse, and is calculated through $(\frac{H_{irr}}{H_m})^2 + (\frac{B}{B_m})^2 = 1$, where $H_m = \frac{k_h B_m}{x}$, B is the flux density and B_m is the amplitude of a minor BH loop obtained through continuously updated magnetic flux density information history. In [28], it is shown that $x = \pi$ given sinusoidal excitation. C_t can be found by utilizing the fact that the iron losses calculations should yield the same value in both frequency and time domain, and the coefficients can therefore be determined by equaling the equations from both domains [28], for known loss values in the frequency domain. In FEM calculations, (8) can then be transformed into its separate x, y, z-components (9)-(11).

$$p_h(t) = \{|H_{irr,x}\frac{dB_x}{dt}|^{\frac{2}{\beta}} + |H_{irr,y}\frac{dB_y}{dt}|^{\frac{2}{\beta}} + |H_{irr,z}\frac{dB_z}{dt}|^{\frac{2}{\beta}}\}^{\frac{\beta}{2}} \tag{9}$$

$$p_c(t) = C_{t,1}\{(\frac{dB_x}{dt})^2 + (\frac{dB_y}{dt})^2 + (\frac{dB_z}{dt})^2\} \tag{10}$$

$$p_e(t) = C_{t,2}\{(\frac{dB_x}{dt})^2 + (\frac{dB_y}{dt})^2 + (\frac{dB_z}{dt})^2\}^{0.75} \tag{11}$$

For 2D-simulations, the z-component is set to zero, eliminating the last term in (9)-(11).

3. Method

3.1. WLTP load torque with Energy Center of Gravity

WLTP drive cycle data were used in this study. Only positive acceleration has been investigated, meaning that all aspects of deceleration and regenerative braking have been excluded.

This study used vehicle parameters typical of a standard large EV [29], as shown in Table 1. The total traction force acting on the vehicle, F_t, was estimated using (12)-(16), and consists of four force components: acceleration force, F_a, drag force, F_d, rolling resistance, F_r, and grading force, F_g [30].

$$F_a = m\frac{d}{dt}v_{car} \tag{12}$$

$$F_d = \frac{1}{2}\rho_a C_d A_f (v_{car} - v_{wind})^2 \tag{13}$$

$$F_r = C_r mg\cos(\alpha) \tag{14}$$

$$F_g = mg\sin(\alpha) \tag{15}$$

$$F_t = F_a + F_d + F_r + F_g \tag{16}$$

where m is the curb weight of the vehicle together with driver weight, v_{car} is the vehicle speed, ρ_a is the density of air, C_d is the drag coefficient and A_f is the effective cross-sectional area of the vehicle. v_{wind} is the parallel or antiparallel component of the wind speed in the direction of the vehicle, although here, the wind speed effect has been excluded, meaning $v_{wind} = 0$. C_r is the rolling resistance coefficient and α is the inclination angle. WLTP does not consider road inclination, resulting in $F_g = 0$ and $F_r = C_r mg$. (17)-(18) were then used to calculate motor load torque values, T_L, as well as rotational speeds of the rotor, w_r.

$$T_L = \frac{F_t r_{wheel}}{n_g \eta_n} \tag{17}$$

$$w_r = \frac{v_{car}}{3.6 r_{wheel}} n_g \tag{18}$$

Table 1
Vehicle parameters [29], [31], [10].

Parameter	Large EV
Curb weight + driver m (kg)	1700 + 75
Front area A (m^2)	2.3
Aerodynamic drag coefficient C_d	0.29
Rolling resistance coefficient C_r	0.007
Wheel radius r_{wheel} (m)	0.312674
Bearing friction coefficient, μ_r	0.002

Table 2
Machine parameters, based on Toyota Prius 2010 [32], [10].

Machine parameter	Value
Stator outer diameter (m)	0.264
Stator inner diameter, D_i (m)	0.1619
Stack length (m)	$50.8 \cdot 10^{-3}$
Number of poles	8
Number of stator slots	48
Stator slot height (m)	$30.9 \cdot 10^{-3}$
Stator slot opening width (m)	$1.88 \cdot 10^{-3}$
Stator tooth width (m)	$7.55 \cdot 10^{-3}$
Airgap length, l_{air} (m)	$0.73 \cdot 10^{-3}$
Magnet dimensions (m)	$49.3 \cdot 10^{-3}$ $\times 17.88 \cdot 10^{-3}$ $\times 7.16 \cdot 10^{-3}$
Number of coils per slot	1
Number of turns per coil	11
Number of parallel paths	1
Number of series turns per phase	88
Stator phase resistance 25 °C, R_a (Ω)	0.077
Type of iron	M19_29G
Iron loss coefficients:	
Eddy current loss coefficient, k_c ($A^2s^3kg^{-1}m^{-1}$)	0.211218
Hysteresis loss coefficient, k_h ($A^2s^2kg^{-1}m^{-1}$)	156.32
Excess loss coefficient, k_e ($A^{1.5}s^{1.5}kg^{-0.5}m^{-1}$)	6.2369
Type of magnet	N36Z
Stator iron mass, m_{stator} (kg)	10.37
Rotor iron mass, m_{rotor} (kg)	6.7
PM mass, m_{PM} (kg)	0.775
Total motor mass (kg)	20.75
Gear ratio, n_g	8.6
Reduction gear efficiency, n_n	0.99
Bus voltage*, V_{DC} (V)	800

*Original bus voltage for Toyota Prius is 650 V.

where r_{wheel} is the wheel radius, see Table 1. n_g is the gear ratio and η_n is the gear axle efficiency. Both can be found in Table 2.

The dynamics of electromagnetic torque, T_e, is explained with (19), and was used to determine the motor torque for each operating point.

$$T_e - T_L = J\frac{d\omega_r}{dt} + \mu_r\omega_r \tag{19}$$

with T_L being load torque, J the inertia coefficient and μ_r the bearing friction coefficient, the latter can be found in Table 1. The change in inertia could be left out in the calculation of electromagnetic torque, and instead be included in the dynamic model simulations. However, since the model in this study operates in a semi-steady state with no net-change in velocity of the rotor, this still needs to be included in the torque calculation in order to take the change in inertia into account. J should normally include all rotating parts, including wheels, gears and motor throughout the power train. Due to limited available data, in this study it was approximated to only constitute the rotor. Magnet and rotor steel material densities are similar, leading to an evenly distributed weight in the rotor, and simplified the calculation of the motor inertia, J, as (20), see Table 2.

$$J = \frac{1}{2}(m_{PM} + m_{rotor}) \cdot (\frac{(D_i - l_{air})}{2})^2 \tag{20}$$

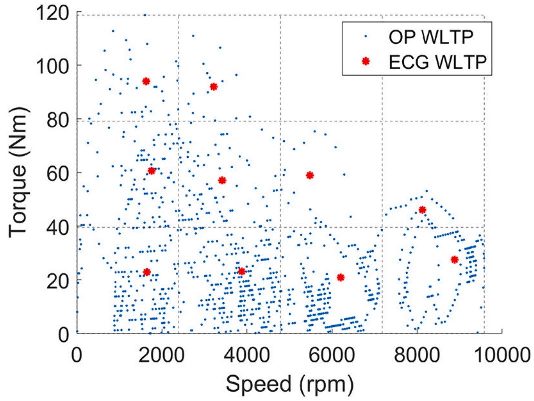

Fig. 1. WLTP operating points (OP) along with resulting Energy Center of Gravity (ECG) grid and points.

Equations (12)-(20), together with WLTP data, determined the motor torque and speed demands, and the established operating points were then quantified using ECG.

ECG utilizes an energy weighted average to find the operating points within a specified sub-region, using (21)-(23), centered in the points ω_{mci} and T_{mci} [11]. All points within the different subregions are combined into one point per subregion. Compared to a method which uses the average speed and torque, ECG shifts the operating point towards speed and torque values where most of the energy is located.

$$E_i = \sum_{j=1,2...}^{N_i} E_{ij} \tag{21}$$

$$\omega_{mci} = \frac{1}{E_i} \sum_{j=1,2...}^{N_i} E_{ij}\omega_{mij} \tag{22}$$

$$T_{mci} = \frac{1}{E_i} \sum_{j=1,2...}^{N_i} E_{ij}T_{mij} \tag{23}$$

where N_i is the number of operating points and E_i is the total energy within the specified grid sub-region.

The energy distribution factor, ϵ_d, how much of the total energy is distributed within each sub-region, can be calculated by dividing the total energy within one grid, E_i, by the sum of the energy for all regions, E_{tot}, see (24).

$$\epsilon_{d,i} = \frac{E_i}{E_{tot}} \tag{24}$$

In the original study of ECG [11], six energy-intensive operating points were identified. The operating region was then divided into six subregions and ECG points were calculated from the remaining operating points, excluding the six energy-intensive points, leading to 12 evaluated points in total. The energy-intensive points arose because in the original study, the NEDC drive cycle was used, where the energy is more concentrated since this drive cycle is less dynamic than WLTP. The total energy loss difference between full drive cycle and the ECG method was 2.1%. For this study, since WLTP is used as the drive cycle and the operating points are more evenly divided, no energy-intensive points were used on their own. Instead, the operating region, defined by limits of maximum torque and speed, was divided into 12 subregions, of which only 10 contained points. A previous study performed by the authors [10], showed the effects of quantification for the same machine design as in this study using the WLTP drive cycle. Even if a different quantification method was used, the effect of quantification on losses and efficiency seems to be minimal even at high levels of quantification, and 12 subregions were deemed enough for the purpose of this study. The WLTP operating points are visualized in Fig. 1, along with the grid used to divide the operating region and the ECG points.

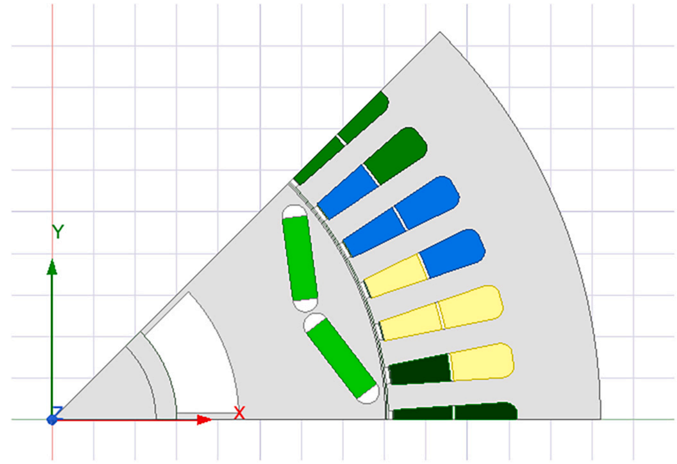

Fig. 2. FEM model of motor based on Toyota Prius 2010, with modifications.

3.2. PMSM model

The motor, based on the 2010 Toyota Prius, was chosen due to the existence of well-documented parameters for this machine. The motor was modeled in Ansys Maxwell 2D, using the parameters shown in Table 2.

The original motor is skewed by 7.5. This can be achieved in Ansys Maxwell 2D by running multiple simulations where the rotor position is shifted in the rotational direction between simulations. However, this will increase simulation time linearly to the number of skew layers and was deemed unnecessary for this study. The choice was therefore made to split the slots into two winding layers and change the slot pitch to 150 degrees compared to its original 180 degrees, in order to achieve the effect of reduced harmonics. The motor model can be seen in Fig. 2. The impact on the maximum torque ripple for this machine by changing the slot pitch was found to be small, and not comparable to using skew, although it almost completely eliminated the sixth harmonic.

One important aspect of optimal motor control, especially for interior-mounted permanent magnet synchronous motors (IPMSMs), is achieving correct estimates of inductance and flux linkages. Given that the magnitude and angle of the current directly influence both flux linkage and inductance, one way to solve this is by creating look-up tables (LUTs). In this study, the Ansys Maxwell 2D was used to run a parametric study, for one quarter of a mechanical rotation, varying the RMS current magnitude from 0 to 200 A and the phase advance angle from 0 to 90 degrees with steps of 10 A and 10 degrees, respectively, for each simulation. With these LUTs, inductance and flux linkage values could be retrieved during the simulations, using linear interpolation.

Higher data resolution LUTs, as well as correct choice of interpolation method together with introducing a third axis for rotor angular position, will likely yield better results, although it increases simulation time, as investigated in [33]. Increased accuracy in these inductance and flux linkage interpolations will allow for better initial estimations of voltages in the model, as well as better decoupling between d- and q-axis voltage in the current control method, at the cost of more computer processing. In a real-life scenario this also increases the need for a more exact knowledge of rotor position, in order to fully achieve the gains of high granularity.

3.3. Model description

A control interface was built using MATLAB and Simulink. Ansys Twin Builder was used to connect the FEM simulations in Ansys Maxwell 2D with the control system in Simulink. In Twin Builder it is possible to extract torque, currents, voltages, back-emf and copper and iron losses from the FEM simulations in Maxwell 2D, as well as apply excitation voltages on the FEM model. Twin Builder could then send these values

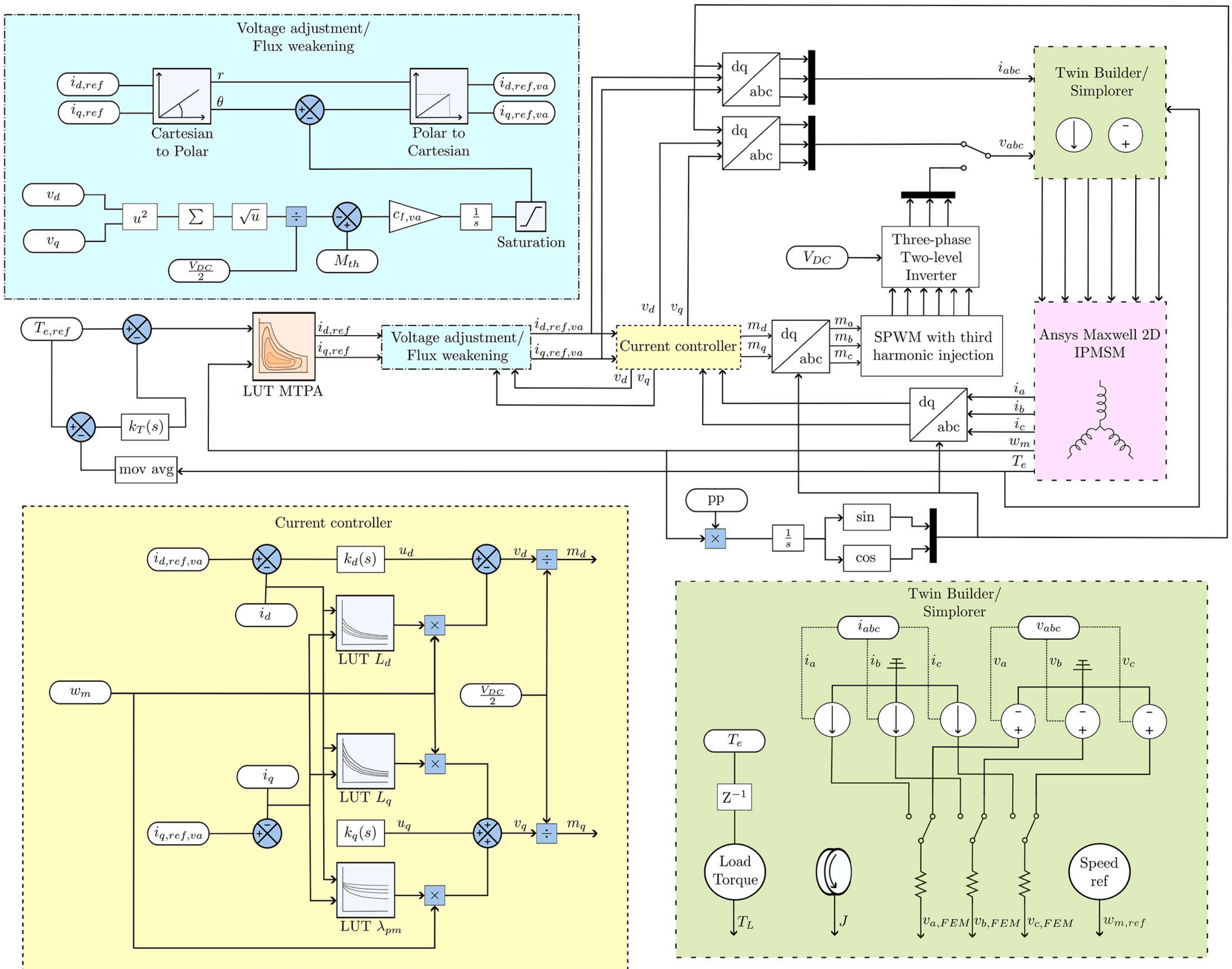

Fig. 3. Full model schematic. The blocks in the white background, along with the blue and yellow squares, are constructed within Simulink, the green square is implemented in Twin Builder/Simplorer and the pink square is the FEM model in Ansys Maxwell 2D, see Fig. 2.

to the control system in Simulink, and Simulink/MATLAB was also used to store and display the results. Twin Builder has also been used to add the inertia, load torque and initial speed of the electric machine, all of which can also be managed via the control system in Simulink. The full model can be seen in Fig. 3. The physical switches indicate where the model changes when different control modes, current source (CS), voltage source (VS) and switching, are activated.

A three-phase two-level inverter was constructed in Simulink, using ideal components. Since this study only evaluates motor losses, all components of the inverter and the connecting cables were assumed to be free from losses. The voltage and current outputs of this inverter were then sent to Twin Builder using the co-simulation interface, where they controlled ideal voltage and current sources. The outputs from these sources were transferred to the FEM model. The current level control method used in the Simulink model for this study was maximum torque per ampere (MTPA). A common way to utilize MTPA is to transform the voltages and currents into their dq components [34], [35], using (25)-(28).

$$i_d = -|i_s| sin\alpha \tag{25}$$

$$i_q = |i_s| cos\alpha \tag{26}$$

$$v_d = R_s i_d + L_d \frac{di_d}{dt} - \omega_e L_q i_q \tag{27}$$

$$v_q = R_s i_q + L_q \frac{di_q}{dt} + \omega_e L_d i_d + \omega_e \lambda_{PM} \tag{28}$$

where i_d and i_q are the dq-current magnitudes, i_s the stator current, α is the current phase advance angle, which here has been defined as the angle between the q-axis and the direction of the current, v_d and v_q are the dq-voltages, R_s is the stator winding phase resistance, L_q and L_d are the q-axis and d-axis inductances and λ_{PM} is the flux linkage originating from the permanent magnets.

The generated electromagnetic torque, expressed in the dq reference frame, can be calculated using (29).

$$T_e = \frac{3}{2} pp(\lambda_{PM}(i_d, i_q) i_q + (L_d(i_d, i_q) - L_q(i_d, i_q)) i_d i_q) \tag{29}$$

where pp is the number of pole pairs.

There are restrictions on maximum current, i_s, and voltage, v_s, due to inverter and control methods along with motor limitations, given by (30) and (31).

$$i_s = \sqrt{i_d^2 + i_q^2} \leq i_m \tag{30}$$

$$v_s = \sqrt{v_d^2 + v_q^2} \leq v_m \tag{31}$$

Table 3
Simulink control system parameters.

Parameter	Value
M_{th}	0.99
$c_{I,va}$	100
R_s	0.1
L_d	$2 \cdot 10^{-3}$
L_q	$5 \cdot 10{-}3$
$c_{P,id}$	4
$c_{I,iq}$	200
$c_{P,iq}$	10
$c_{I,iq}$	200
σ	$5 \cdot 10^{-4}$
$c_{P,T}$	2
$c_{I,T}$	100

Table 4
Ansys Machine Toolkit input parameters.

Parameter	Input
Voltage control	Third harmonic PWM
Control Strategy	MTPA
Connection type	Wye
Number of electric periods simulated	1
Number of time steps per period	30
Number of periods used for average	1
Number of current sweep points	10
Number of angle sweep points	10
Number of speed sweep points	10
Phase resistance (Ohm)	0.1
End winding inductance (mH)	0

$$v_m = \frac{V_{DC}}{2} \tag{32}$$

where V_{DC} here is simplified to be the battery voltage. For these calculations, no voltage drop over the inverter is included since ideal power electronic components are assumed.

Both the phase advance angle of the current and its magnitude influence the generation of torque, as seen in (29). To achieve optimal dq-currents according to MTPA, for the torque and speed values requested, a torque/speed/current LUT was created and utilized.

The voltage adjustment/flux weakening block is activated when the average voltage level increases above the allowed limit, set by the modulation index M_{th}. It changes the relation between i_d and i_q, to keep the voltage as close to the set limit as possible. The dq-currents are transformed into polar coordinates. When the calculated motor voltage is higher than the limit set by the inverter restrictions and modulation index, d-current is increased to lower induced voltage in the motor. The torque controller makes sure to keep the torque at the set target value.

PI controllers were used to maintain torque and dq-current values. By rewriting (27)-(28), and introducing the new control variables $u_d = \omega_e L_q i_q + v_d$ and $u_q = \omega_e L_d i_d - \omega_e \lambda_{PM} + v_q$, we get two decoupled, first order subsystems (33)-(34), which forms the basis for the PI controllers.

$$u_d = R_s i_d + L_d \frac{di_d}{dt} \tag{33}$$

$$u_q = R_s i_q + L_q \frac{di_q}{dt} \tag{34}$$

The PI gains can then be found through the $c_P = \frac{L}{\sigma}$ and $c_I = \frac{R_s}{\sigma}$, where c_p and c_I are the PI controller values for proportional and integral gain respectively, and σ is the time constant.

A constant temperature of 100 °C was assumed for all evaluated operating points. Resistance data for the Toyota Prius 2010 is available at 25 °C from [32], and the new resistance at 100 °C was calculated to 0.1 Ω.

As was mentioned previously, L_d and L_q change both with regards to saturation and rotor position, they are functions of current magnitude and phase advance angle. However, during model testing variable PI gains were noticed to introduce some instabilities during fast changes in currents, and the gains were therefore set as fixed throughout all operating points. The values, as well as resulting values for $c_{P,i}$ and $c_{I,i}$ for both d- and q-current, can be seen in Table 3. The time constant, σ, was set to $5 \cdot 10^{-3}$, 10 times larger than the 5 kHz switching frequency used in the model, to not have the PI controller react strongly on inverter switching.

Control models can be based on either speed or torque reference values. The model can be operated using both methods, however, for this study a torque control method was implemented. The model can be described with two loops, the outer one containing either the torque or speed control, and the inner controls dq-currents. To avoid having the model react to torque ripple, a moving average filter was implemented, with a sliding window length covering one electrical period. The PI controller proportional and integral gains, $c_{P,T}$ and $c_{I,T}$, can be seen in Table 3.

AMT can be used to generate efficiency curves, as well as the corresponding dq-currents. Torque/speed-to-current LUTs for a sweeping range of torque and speed values were created using these, and were used in the control model, see Fig. 3. The input parameters for this toolkit can be seen in Table 4.

The operating point current values for each respective torque and speed value, calculated using ECG, were used as initial values in the model. A PI controller was then utilized to adjust the torque level, when the torque target given from the torque/speed-to-current LUTs varied from the target torque. Since the model was run in a semi-stable state, meaning that no change in rotational speed was necessary, this regulation was not optimized. Instead, the parameters for the torque PI controller were chosen to provide a stable output within a reasonable time frame.

It is possible to choose different operating modes and inverter control methods in the model. The methods used in this study are ideal sinusoidal CS and ideal VS control, as well as sinusoidal pulse width modulation (SPWM) voltage control. For the previous two systems, the inverter is disconnected and the current and voltage sources are directly controlled with control system output. The switching frequency for SPWM was also adjusted, and switching frequencies of 2 kHz, 5 kHz and 10 kHz were implemented. A higher switching frequency is possible to implement; however, this could impact the need for higher sampling frequency, which directly impacts the simulation time. The sampling frequency, f_s was fixed during all tests and set at 200 kHz, which was chosen to be fast enough to not have a too large impact on the results [36], while still minimizing the simulation time. The choice of sample frequency for real-life applications is usually set by equipment restrictions and control optimization, and will have a distinct impact on losses [14].

When running the machine with an ideal CS the model can no longer regulate optimally regarding voltage, since the instantaneous inductances are unknown in the model, which creates some comparison dilemmas for this case. Therefore, the choice was made to fix the current in the d-axis to provide a realistic and sufficient flux weakening, and only allowing the current in the q-axis to vary to achieve the wanted torque. CS and VS are therefore run as two different simulations.

Several different methods have been used to decrease model simulation time. Since steady-state operating points are investigated, the different operating point speeds could be used directly as the initial speed. During initialization and before model stabilization, it is possible for the simulation to experience high values of current and torque. In order to assure model and speed stability during the first simulation period, as well as to limit simulation time, the inertia of the machine was increased manifold during initialization. This was also implemented during switching of control mode, since a similar, although often smaller, fluctuation of current and torque can be experienced. By increasing the inertia, this ensures that the correct speed is still maintained. The inertia was then gradually decreased to its actual value once the model had stabilized. This greatly reduced simulation time and increased model stability, and proved to be a good method to make dynamic co-simulations more achievable. A second method utilized in this study was to provide precise initial currents estimations, found through AMT efficiency map creation. Through this, the control model has a fairly accurate starting point. Third, by initializing the model with a CS as the power source and estimating correct voltages, the model can more quickly stabilize, and when later changing to a voltage driven system and implementing switching the control system is already close to the correct values, greatly reducing simulation time. The final action taken was to apply an average load torque calculated from the actual motor torque achieved. This, in combination with high inertia for model initialization and switching steps, created a more stable simulation, and this method automatically tunes itself.

3.4. Losses and efficiency

Copper losses for each respective sub-region in the ECG grid were calculated using (35).

$$P_{cu,i} = \frac{3}{2} R_s \left(\sqrt{i_{d,i}^2 + i_{q,i}^2}\right)^2 \tag{35}$$

Given the stranded nature of the windings of the Toyota Prius 2010, AC copper losses have been excluded, although it is possible to activate these calculations, allowing Ansys Maxwell to calculate both DC and AC copper losses.

Iron losses for each evaluated operating point, $P_{ir,i}$, were simulated in Ansys Maxwell 2D. Average values for both copper and iron losses for two electric periods, once the motor control model had stabilized, were then calculated. Constant iron loss coefficients were provided through the Ansys material database and these were used in the calculation of iron losses, with values given in Table 2, both for transient simulations and for AMT, to make the different methods comparable. A loss correction factor is often used, to decrease the mismatch between calculated or simulated values and real-life measurements. In this study, it was set to 1.7 for all control modes, as well as for AMT.

Potential magnet loss can be calculated using Ansys Maxwell. It was excluded from the study, since this will demand a higher mesh density inside the magnets and increase simulation time.

The complete drive cycle efficiency could then be calculated using (36).

$$\eta = \sum_{i=1,2...}^{N_o} \epsilon_{d,i} \frac{T_{mci}\omega_{mci}}{T_{mci}\omega_{mci} + P_{cu,i} + P_{ir,i}} \tag{36}$$

4. Results and discussion

The choice of motor design was justified by two different arguments. Firstly, the motor is well documented and studied, regarding both machine parameters and performance. Secondly, this study is meant to show the importance of dynamic loss and efficiency simulations and not to evaluate a specific motor type. By using a well-documented machine, it simplifies comparisons with other studies and enables easier verification from additional sources.

Motor losses and efficiency are often displayed using so-called efficiency maps, limited by a torque/speed curve. Since only 10 points have been analyzed in this study, this is not possible. However, the energy density for these operating points along with the respective efficiency of each point has been visualized in Fig. 4. This case is when the motor is run with ideal sinusoidal currents, which is used as the reference case when comparing the other control modes. It can be seen that most of the energy is located in the bottom right and also in the middle of the drive cycle.

The current ripple magnitude for operating point 1 and 9, compared to using an ideal CS, is displayed in Figs. 5-6. As expected, we see an increase in current ripple when switching is introduced. For low speeds we see that even lower switching frequencies manage to keep the current quite stable. For high speeds this is no longer the case, and the current waveform sees a large degree of instability.

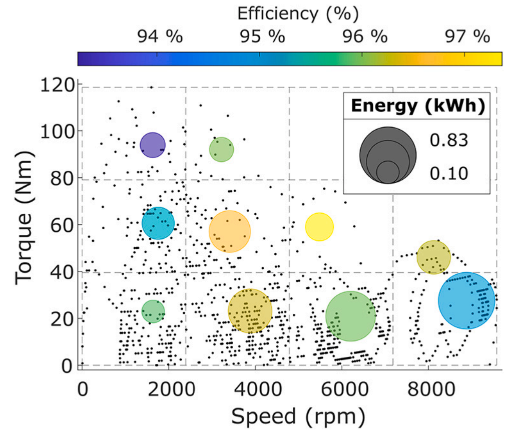

Fig. 4. ECG energy distribution for WLTP and resulting efficiency using an ideal sinusoidal current source.

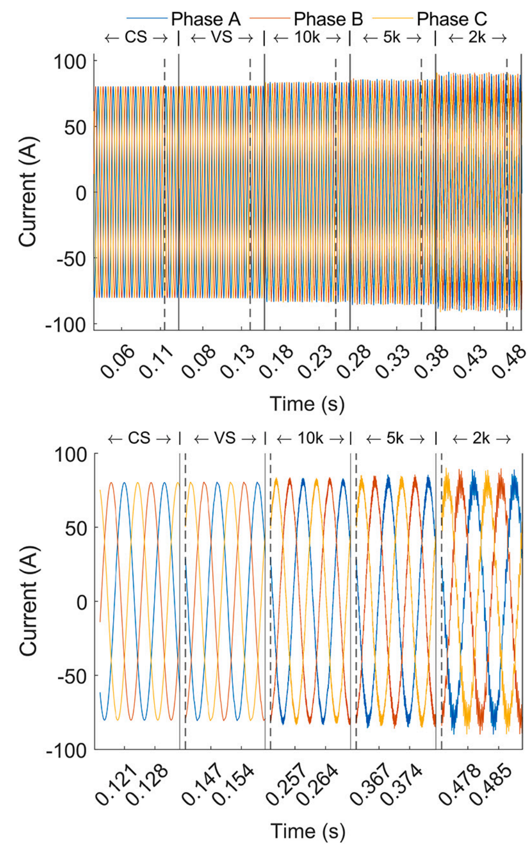

Fig. 5. Phase currents for different supply methods, ideal sinusoidal current source (CS), ideal voltage source (VS) and switching frequencies 10 kHz (10k), 5 kHz (5k) and 2 kHz (2k) for operating point 1 and zoomed in on sample area.

The model torque response and the resulting copper losses, iron losses and efficiency for operating point 1 and 9 respectively can be seen in Figs. 7-8. Here the impact of the current ripple can clearly be seen. Torque ripple increases with both an introduction to switching, as well as decreasing the switching frequency, which is to be expected. It is however interesting to see that torque ripple actually lowers when the ideal VS is used.

The impact on copper losses is relatively low regardless of control method, except for very low switching frequencies and higher speeds. For iron losses there is a large increase when switching is initiated, with

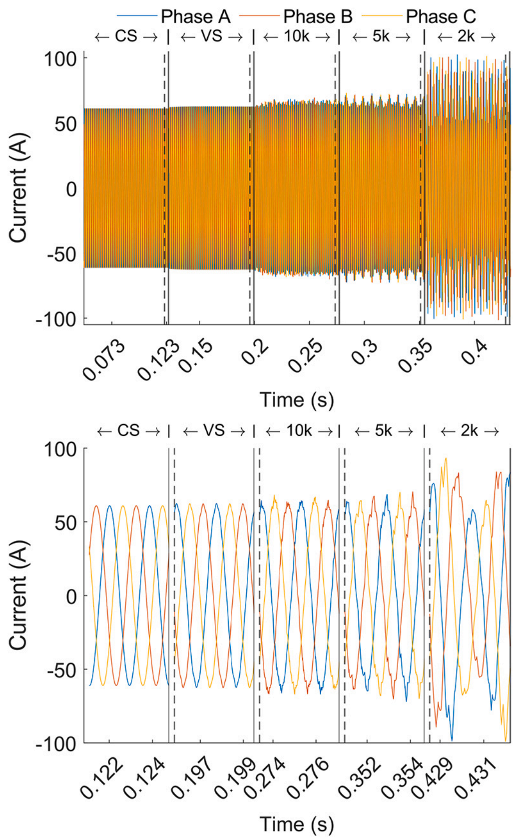

Fig. 6. Phase currents for different supply methods, ideal sinusoidal current source (CS), ideal voltage source (VS) and switching frequencies 10 kHz (10k), 5 kHz (5k) and 2 kHz (2k) for operating point 9 and zoomed in on sample area.

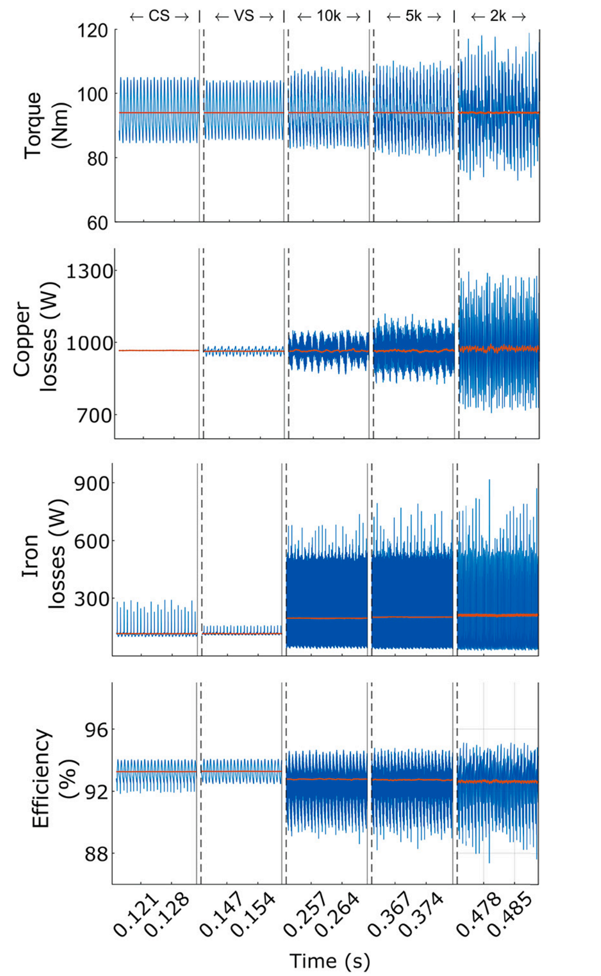

Fig. 7. Torque, losses and efficiency for different control methods, separated by solid vertical lines, including ideal sinusoidal current source (CS), ideal voltage source (VS) and switching frequencies 10 kHz (10k), 5 kHz (5k) and 2 kHz (2k), for operating point 1. Instant values are shown with blue lines, while moving average values over half an electric period are marked with orange.

lower speeds being more affected. For point 9, at high speeds, we can see that the control system is struggling to keep the average torque stable, due to the high content of current harmonics, which greatly affects both copper and iron losses. The torque ripple is also affected, and we see a larger percentage of increase for low switching frequencies at higher speeds. These effects could possibly be reduced by fine-tuning of the control system, and reducing the current controller PI gains, although the latter would result in a slower control.

The results from the different control methods can be seen in Table 5. Copper losses are not majorly impacted by the introduction of switching, nor by the switching frequency. Although, we can see large increase in copper losses for the lowest switching frequencies, caused by the large current harmonics, especially at high speeds. Multiple case studies have tested the impact of switching frequency. In [14], motor iron losses decrease with an increase in switching frequency, until approximately 100 kHz, which is much higher than the frequencies investigated in this study. Similarly, in [15], the same pattern can be seen, although here the total losses are recorded. In [16], where FEM simulations and experimental testing were both carried out for a single operating speed and two torque values, it can clearly be seen that low switching frequency, 2.5 kHz, has a large impact on the losses, with both 5 kHz and 10 kHz having losses approximately 25-30% lower for low torque operation. A sinusoidal voltage supply also reduced losses with an additional 15%. In our study, the impact on the copper losses is minor until higher speeds are reached, even for low switching frequencies. One explanation for this could be due to differences in machine design and their inductance values, which would change how switching frequency impacts current harmonics. This could explain why large differences in copper losses are only seen for higher speeds in our study.

What is interesting to observe is that the copper and iron losses are lower for a switching frequency of 5 kHz than it is for 10 kHz at high speeds, which also corresponds well to the experimental results in [16]. Above base speed, we notice that the decrease in frequency actually reduces the average current needed to produce the necessary torque. Fig. 9 shows the changes in current magnitude for operation point 7, and it is clear that the average currents are lower for switching frequencies of 5 kHz and 2 kHz compared to 10 kHz. The reduced average current lowers the copper losses.

However, the reduction is limited by the increase in current harmonic content, seen in the results from a total harmonic distortion (THD) analysis shown in Table 5, and larger current peaks at high speeds, as seen in Fig. 6. THD has been calculated for current and torque using equation (37).

$$THD = \sqrt{\sum_{j=2}^{N}(\frac{h_j}{h_1})^2} \cdot 100\% \tag{37}$$

where h_j is the magnitude of the different harmonic components, and when looking at current THD, h_1 is the magnitude of the fundamental, and for torque THD, h_1 is the average torque component. Low torque and high speeds seem to especially affect current THD when switching frequency is lowered. However, the relative change in current THD seem to be more stable between the points, and for example operating point 3, which has the highest THD for all low speed operating points, actually experiences the lowest relative change when switching frequency

Table 5
Drive cycle control method evaluation for Ansys Machine Toolkit (AMT), Current Source (CS), Voltage Source (VS) and switching frequencies 10 kHz, 5 kHz and 2 kHz.

Operating point ECG	Method	1	2	3	4	5	6	7	8	9	10
Speed (rpm)		1632.0	1757.9	1641.5	3220.1	3409.3	3882.5	5483.3	6203.4	8121.8	8880.7
Target Torque (Nm)		93.97	60.64	22.93	91.98	57.02	23.16	58.99	20.89	46.00	27.51
Actual torque [average] (Nm)	AMT	93.97	60.64	22.93	91.98	57.02	23.16	58.99	20.89	46.00	27.51
	CS	93.97	60.64	22.93	91.97	57.02	23.16	58.98	20.90	45.97	27.52
	VS	93.96	60.62	22.90	91.95	56.98	23.12	58.90	20.76	46.03	27.51
	10 kHz	93.99	60.67	22.89	91.92	56.99	23.15	58.95	20.91	45.99	27.50
	5 kHz	93.94	60.61	22.97	91.96	57.01	23.14	58.91	20.86	46.04	27.66
	2 kHz	93.93	60.61	22.93	91.98	57.01	23.20	58.99	20.81	45.44	27.82
Power (kW)	AMT	16.06	11.16	3.94	31.02	20.36	9.42	33.87	13.57	39.12	25.58
	CS	16.06	11.16	3.94	31.01	20.36	9.42	33.86	13.57	39.10	25.59
	VS	16.06	11.16	3.94	31.01	20.34	9.40	33.82	13.49	39.15	25.58
	10 kHz	16.06	11.17	3.93	31.00	20.35	9.41	33.85	13.58	39.12	25.58
	5 kHz	16.05	11.16	3.95	31.01	20.35	9.41	33.83	13.55	39.16	25.72
	2 kHz	16.05	11.16	3.94	31.01	20.35	9.43	33.87	13.52	38.64	25.87
Copper losses (W)	AMT	1000.3	441.8	79.9	953.6	397.4	81.4	447.0	69.0	624.8	366.7
	CS	966.2	421.3	73.1	951.6	396.0	75.0	411.3	64.3	558.1	332.8
	VS	963.4	420.1	72.8	946.2	393.9	74.6	410.5	63.8	564.6	336.6
	10 kHz	964.9	421.4	73.2	946.6	394.2	75.4	425.8	67.0	602.2	369.9
	5 kHz	964.7	421.4	73.6	951.1	395.7	75.8	418.0	67.3	587.6	356.1
	2 kHz	973.4	425.8	74.4	974.0	412.6	82.8	449.5	99.9	778.5	494.3
Iron losses (W)	AMT	121.8	116.3	86.9	308.4	285.3	279.8	551.8	531.4	1115.5	1157.7
	CS	115.8	111.3	85.8	283.5	272.5	259.2	469.7	465.3	872.7	896.1
	VS	115.7	110.9	86.2	282.1	271.7	259.5	469.0	461.2	856.3	886.1
	10 kHz	195.8	190.1	155.5	385.7	375.1	354.6	543.3	525.2	934.5	968.3
	5 kHz	201.6	195.0	155.2	394.2	380.1	364.4	551.0	539.6	930.1	957.6
	2 kHz	210.2	200.8	159.4	399.9	385.4	363.0	563.9	547.5	1026.3	1034.7
Efficiency (%)	AMT	93.44	95.15	95.50	96.06	96.65	95.82	97.07	95.10	95.65	94.00
	CS	93.23	95.19	95.85	96.00	96.70	96.35	97.37	95.95	96.26	94.93
	VS	93.25	95.20	95.82	96.02	96.71	96.31	97.37	95.92	96.30	94.98
	10 kHz	92.75	94.50	94.05	95.69	96.20	95.30	97.11	95.43	95.98	94.51
	5 kHz	92.72	94.46	94.06	95.65	96.17	95.17	97.10	95.30	96.03	94.63
	2 kHz	92.64	94.38	93.94	95.56	96.06	95.08	96.97	94.78	95.08	93.62
Torque ripple compared to CS (%)	AMT	N/A	N/A	N/A	N/A	N/A	N/A	N/A	N/A	N/A	N/A
	CS	0.00	0.00	0.00	0.00	0.00	0.00	0.00	0.00	0.00	0.00
	VS	-9.1	-13.8	-5.0	-13.2	-14.5	-4.8	-12.7	-2.7	-5.1	-5.5
	10 kHz	29.5	31.2	17.5	17.7	12.2	20.7	19.9	16.4	11.8	13.2
	5 kHz	46.6	43.1	25.0	37.8	50.8	29.2	19.0	22.9	31.9	15.2
	2 kHz	127.8	116.4	57.4	130.9	117.4	95.8	78.6	114.5	121.3	111.6
Torque THD (%)	AMT	N/A	N/A	N/A	N/A	N/A	N/A	N/A	N/A	N/A	N/A
	CS	9.77	13.8	26.4	10.1	13.6	26.5	14.7	28.7	18.4	26.9
	VS	8.98	12.1	25.0	8.94	12.1	25.4	13.0	27.6	17.5	25.0
	10 kHz	9.66	13.2	26.0	9.32	12.7	25.0	14.2	28.6	17.7	25.2
	5 kHz	10.1	13.5	26.2	9.89	13.5	26.4	13.9	28.1	19.3	25.9
	2 kHz	13.4	17.7	29.4	14.6	19.2	32.7	18.0	36.7	25.5	36.9
Current THD (%)	AMT	N/A	N/A	N/A	N/A	N/A	N/A	N/A	N/A	N/A	N/A
	CS	0.00	0.00	0.00	0.00	0.00	0.00	0.00	0.00	0.00	0.00
	VS	1.00	1.64	2.74	1.33	1.94	3.11	1.61	3.24	1.77	1.63
	10 kHz	2.64	3.78	7.41	3.58	4.75	8.24	4.58	9.52	3.39	3.95
	5 kHz	3.93	5.02	7.27	5.91	7.11	11.2	7.25	16.8	6.41	8.22
	2 kHz	9.19	11.7	14.7	13.1	19.1	30.5	20.9	47.7	15.9	23.4

decreases, see Fig. 10. Speed seems to have a more direct impact on relative current THD, although no absolute relationship can be discerned from the results.

Relative torque ripple, $T_{rip,CM}/T_{rip,CS}$, where $T_{rip} = \frac{T_{max}-T_{min}}{T_{avg}} \cdot 100\%$ and CM indicates the different control modes, increases when switching is introduced, and further increases when lowering the switching frequency. The largest relative increase for this study can be seen for high torque values, for example operating point 1 and 4, although an increase is also clearly visible for higher speeds, meaning that high accuracy machine performance evaluation becomes more important if a large amount of energy is centered in either high torque or high speed operating points, if torque ripple is a determining design factor. Although, an interesting aspect is that even though the torque ripple changes drastically between the control methods, the THD for the torque only differed slightly for most control modes, with the one exception being switching frequencies of 2 kHz, see Table 5.

Fig. 11 shows the overall drive cycle efficiency for all evaluated methods. The drive cycle efficiency of AMT is very similar to the efficiency for the control methods using higher frequency switching, 10 kHz and 5 kHz, which could indicate that this method is good enough to perform drive cycle analysis. However, when we look more deeply into the different losses in Table 5 we see that AMT overestimates the copper losses while underestimating iron losses, which could have a very large impact if different motor designs or drive cycles are evaluated.

It can also be seen that the overall drive cycle efficiency for both 10 kHz and 5 kHz is identical. Even if small variations can be seen in Table 5, this shows that if the increase in torque ripple is acceptable, the overall drive train efficiency could be increased by lowering the

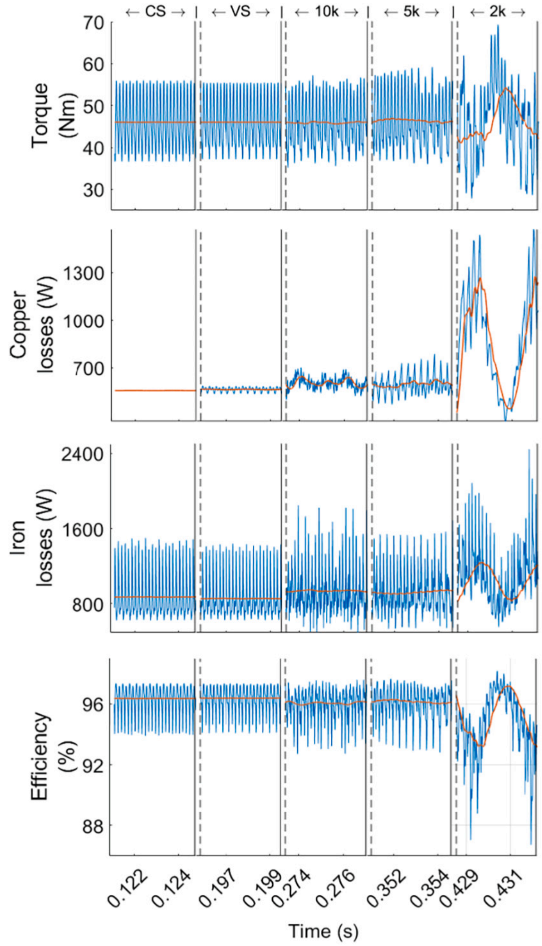

Fig. 8. Torque, losses and efficiency for different control methods, separated by solid vertical lines, including ideal sinusoidal current source (CS), ideal voltage source (VS) and switching frequencies 10 kHz (10k), 5 kHz (5k) and 2 kHz (2k), for operating point 9. Instant values are shown with blue lines, while moving average values over half an electric period are marked with orange.

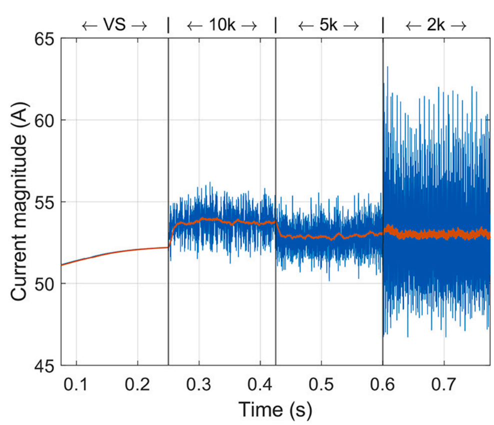

Fig. 9. Current magnitude (blue) and average current magnitude over half an electric period (orange) for operating point 7 for different control methods: Voltage Source (VS), switching frequencies 10 kHz (10k), 5 kHz (5k) and 2 kHz (2k).

switching frequency, since this would lower the switching losses in the inverter.

It was also discovered that the dq-currents from the 2D current LUTs generated from the AMT results did not yield correct torque values in the dynamic model, especially at higher speeds. We also see an increased discrepancy for low torque values. The values and the difference in actual torque and target torque can be seen in Table 6. This error can lead to inaccuracies in motor performance estimation, and in real driving scenarios an unoptimized control and larger losses. A possible way to reduce the error could be to use higher granularity LUTs, or by introducing a third axis which also takes rotor position into consideration, although this will increase simulation time.

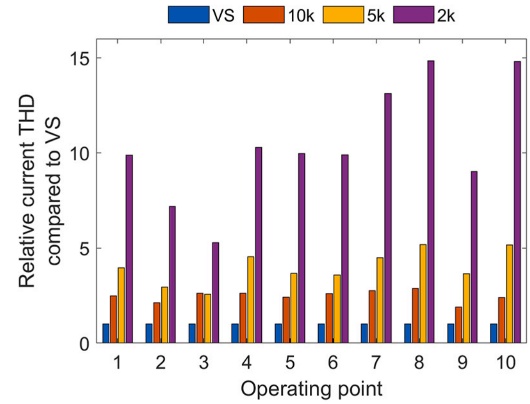

Fig. 10. Relative THD content for currents at different switching frequencies, 10 kHz (10k), 5 kHz (5k) and 2 kHz (2k), compared with voltage source (VS).

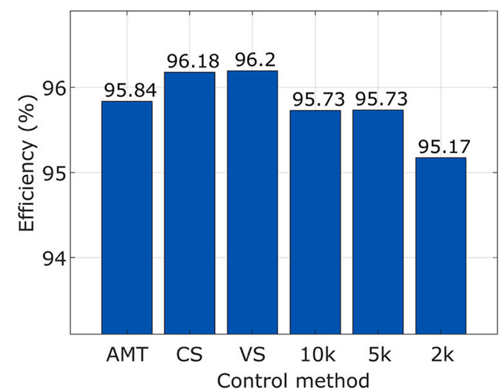

Fig. 11. Full drive cycle efficiency for all methods, Ansys Machine Toolkit (AMT), ideal sinusoidal current source (CS), ideal voltage source (VS) and switching frequencies 10 kHz (10k), 5 kHz (5k) and 2 kHz (2k), utilized in this study.

Table 6
Unregulated torque from current look-up table compared to target torque.

Operating Point	Actual torque (Nm)	Target torque (Nm)	Difference (%)
1	94.63	93.97	0.70
2	60.80	60.64	0.27
3	21.59	22.93	-5.87
4	91.27	91.98	-0.77
5	55.58	57.02	-2.52
6	21.69	23.16	-6.34
7	60.52	58.99	2.59
8	19.05	20.89	-8.79
9	56.11	46.00	21.99
10	34.76	27.51	26.36

These results show that, even though the overall losses and efficiency stay fairly consistent across the full range of speeds and torques, the use of LUTs and the methods of calculating an efficiency map employed in Ansys Maxwell can lead to errors, especially at high speeds. If that method is to be used, it is important to evaluate the resolution used for the input parameters.

It is important to note that the results shown in this paper are case-specific, both with regards to motor design, control system and choice of evaluation. A change in PI parameters, modulation index or sample time will provide variations on the output, both with regards to current ripple and the resulting losses, although a similar pattern should be visible. Therefore, the developed model should be seen as a tool in how it is possible to evaluate motor design on a deeper level, and it showcases the importance of investigating the impact of switching frequencies for the full vehicle operating range.

Analyzing high-frequency effects using FEM on longer time frames is very time consuming, and dynamic models are therefore seldom used. However, by combining different methods it has been shown in this paper that it is possible, and this allows for a deeper analysis of a motor's design before manufacturing and physical testing. Combining this with a commonly used quantification method has allowed for motor drive cycle analysis. The large discrepancies between the different supply methods show the importance of these studies, and can be used to achieve more accurate and efficient control methods and algorithms, lowering machine losses as well as allowing for more correct sizing of system cooling, since a better estimation of losses is attained.

5. Conclusions

This study shows the importance of evaluating the dynamics of a vehicle powertrain when it comes to motor efficiency. It also demonstrates that it is possible to evaluate the impact of the switching frequency for multiple operating points, as well as how it affects overall drive cycle efficiency.

A dynamic simulation model has been developed consisting of a FEM model that reacts to control input. It has been used to evaluate the impact on a PMSM running the WLTP drive cycle for different power supplies and inverter switching frequencies. The results demonstrate that simulating a motor model with an ideal sinusoidal CS could be insufficient to evaluate the full performance of a drive cycle. Especially if the ratio between the motor and the switching frequency becomes too low, for example if the motor is expected to run at high speeds or a lower switching frequency is used.

It is clear that switching has an effect on both losses and torque ripple and that different switching frequencies also affect the overall performance. Introducing switching has a larger impact on iron losses at low speeds, while copper losses see a larger relative increase when the ratio between fundamental rotational frequency and switching frequency becomes too low.

However, the effect by lowering the switching frequency, for this motor and control method, can almost be considered negligible until we reach low switching frequencies. When comparing 10 kHz and 5 kHz, above base speed, the increase in copper losses from current harmonics arising due to lower switching frequencies is compensated by the decrease in current magnitude. This also has other implications; for example, base speed can be somewhat increased by lowering the switching frequency, although further studies on this are necessary. If the increase in torque ripple is manageable, then lower switching frequencies could be beneficial since inverter losses are reduced.

CRediT authorship contribution statement

Emil Lind: Writing – original draft, Software, Methodology, Investigation, Formal analysis, Data curation, Conceptualization. **Sandra Eriksson:** Writing – review & editing, Supervision, Methodology, Funding acquisition, Conceptualization.

Declaration of competing interest

The authors declare that they have no known competing financial interests or personal relationships that could have appeared to influence the work reported in this paper.

Acknowledgements

This research was financially supported by the Swedish Energy Agency, Project No. P51788-1. This work was conducted within the StandUp for Energy strategic research framework.

Data availability

Data will be made available on request.

References

[1] European Environment Agency, Trends and Projections in Europe 2022, Publications Office of the European Union, 2022.
[2] European Environment Agency, Trends and Projections in Europe 2024, Publications Office of the European Union, 2024.
[3] R. S, J. R, Review on electric mobility: trends, challenges and opportunities, Results Eng. 23 (2024) 102631, https://doi.org/10.1016/j.rineng.2024.102631, https://www.sciencedirect.com/science/article/pii/S2590123024008867.
[4] B. Ganji, A.Z. Kouzani, H.M. Trinh, Drive cycle analysis of the performance of hybrid electric vehicles, in: K. Li, M. Fei, L. Jia, G.W. Irwin (Eds.), Life System Modeling and Intelligent Computing, Springer Berlin Heidelberg, Berlin, Heidelberg, 2010, pp. 434–444.
[5] M. Tutuianu, P. Bonnel, B. Ciuffo, T. Haniu, N. Ichikawa, A. Marotta, J. Pavlovic, H. Steven, Development of the world-wide harmonized light duty test cycle (WLTC) and a possible pathway for its introduction in the European legislation, Transp. Res., Part D, Transp. Environ. 40 (2015) 61–75, https://doi.org/10.1016/j.trd.2015.07.011.
[6] A. Chatzipanagi, J. Pavlovic, M. Ktistakis, D. Komnos, G. Fontaras, Evolution of European light-duty vehicle CO2 emissions based on recent certification datasets, Transp. Res., Part D, Transp. Environ. 107 (2022) 103287, https://doi.org/10.1016/j.trd.2022.103287.
[7] E. Carraro, M. Morandin, N. Bianchi, Traction PMASR motor optimization according to a given driving cycle, IEEE Trans. Ind. Appl. 52 (1) (2016) 209–216, https://doi.org/10.1109/TIA.2015.2477479.
[8] X. Zeng, C. Cui, Y. Wang, G. Li, D. Song, Segemented driving cycle based optimization of control parameters for power-split hybrid electric vehicle with ultracapacitors, IEEE Access 7 (2019) 90666–90677, https://doi.org/10.1109/ACCESS.2019.2926504.
[9] G.-h. Lee, Y.-m. You, Efficiency optimization of the main operating points of an ev traction motor, Appl. Sci. 15 (1) (2025), https://doi.org/10.3390/app15010368, https://www.mdpi.com/2076-3417/15/1/368.
[10] E. Lind, D. Bergman, S. Eriksson, Effect of drive cycle quantification on electric motor efficiency, in: 12th International Conference on Power Electronics, Machines and Drives (PEMD 2023), 2023, pp. 96–104.
[11] P. Lazari, J. Wang, L. Chen, A computationally efficient design technique for electric-vehicle traction machines, IEEE Trans. Ind. Appl. 50 (5) (2014) 3203–3213, https://doi.org/10.1109/TIA.2014.2304619.
[12] M. van der Geest, H. Polinder, J.A. Ferreira, Influence of pwm switching frequency on the losses in pm machines, in: 2014 International Conference on Electrical Machines (ICEM), 2014, pp. 1243–1247.
[13] A. Boglietti, P. Ferraris, M. Lazzari, M. Pastorelli, Change of the iron losses with the switching supply frequency in soft magnetic materials supplied by pwm inverter, IEEE Trans. Magn. 31 (6) (1995) 4250–4252, https://doi.org/10.1109/20.489942.
[14] G.M.T. Nguyen, L. Ton-That, K. Fujisaki, Experimental study of mutual effects of high carrier frequency, dead-time and control sample time on ipmsm core loss under sic inverter excitation, Results Eng. 19 (2023) 101278, https://doi.org/10.1016/j.rineng.2023.101278, https://www.sciencedirect.com/science/article/pii/S259012302300405X.
[15] P. Poolphaka, E. Jamshidpour, T. Lubin, L. Baghli, N. Takorabet, Influence of high-frequency operation on the efficiency of a pmsm drive with sic-mosfet inverter, Energies 17 (10) (2024), https://doi.org/10.3390/en17102347, https://www.mdpi.com/1996-1073/17/10/2347.
[16] A. Sarigiannidis, A. Kladas, Switching frequency impact on permanent magnet motors drive system for electric actuation applications, IEEE Trans. Magn. 51 (2015) 1–4, https://doi.org/10.1109/TMAG.2014.2358378.
[17] C. Schulte, J. Böcker, Co-simulation of an electric traction drive, in: 2013 International Electric Machines & Drives Conference, 2013, pp. 974–978.
[18] C. Schulte, J. Böcker, Co-simulation of an interior permanent magnet synchronous motor with segmented rotor structure, in: IECON 2014 - 40th Annual Conference of the IEEE, Industrial Electronics Society, 2014, pp. 437–442.
[19] L. Hölsch, A. Brosch, R. Steckel, T. Braun, S. Wendel, J. Böcker, O. Wallscheid, Insights and challenges of co-simulation-based optimal pulse pattern evaluation for electric drives, IEEE Trans. Energy Convers. 39 (3) (2024) 2094–2105, https://doi.org/10.1109/TEC.2024.3374962.
[20] L. Di Leonardo, M. Popescu, M. Tursini, M. Villani, Finite elements model co-simulation of an induction motor drive for traction application, in: IECON 2019 - 45th Annual Conference of the IEEE Industrial Electronics Society, vol. 1, 2019, pp. 1059–1065.

[21] T.K. Mersha, C. Du, Co-simulation and modeling of pmsm based on ansys software and simulink for evs, World Electr. Veh. J. 13 (1) (2022), https://doi.org/10.3390/wevj13010004, https://www.mdpi.com/2032-6653/13/1/4.
[22] S. Zhao, D. Tian, Y. Ni, Y. Wang, J. Chen, J. Xu, The co-simulation of pmsm control system based on the equivalent circuit extraction model, in: 2023 IEEE 6th International Conference on Electronic Information and Communication Technology (ICEICT), 2023, pp. 541–545.
[23] K.-Y. Hung, N.-W. Liu, S.-C. Yang, A method for constructing synchronous electrical machine equivalent circuit models for motor-drive co-simulation, IEEE Trans. Ind. Appl. (2025) 1–16, https://doi.org/10.1109/TIA.2025.3531828.
[24] W. Li, J. Xue, X. Fan, L. Zhu, Loss analysis of permanent magnet synchronous motor system based on strategy-circuit-field co-simulation and an accurate iron loss calculation method, IEEE Access 12 (2024) 168339–168348, https://doi.org/10.1109/ACCESS.2024.3497941.
[25] I. Talebian, N. Rostami, Co-simulation of a surface-mounted permanent magnet synchronous motor drive using finite element method, in: 2021 IEEE International Power and Renewable Energy Conference (IPRECON), 2021, pp. 1–6.
[26] G. Mörée, M. Leijon, Iron loss models: a review of simplified models of magnetization losses in electrical machines, J. Magn. Magn. Mater. 609 (2024) 172163, https://doi.org/10.1016/j.jmmm.2024.172163, https://www.sciencedirect.com/science/article/pii/S0304885324004542.
[27] B.A. Nasir, An accurate iron core loss model in equivalent circuit of induction machines, J. Energy 2020 (1) (2020) 7613737, https://doi.org/10.1155/2020/7613737, https://onlinelibrary.wiley.com/doi/pdf/10.1155/2020/7613737, https://onlinelibrary.wiley.com/doi/abs/10.1155/2020/7613737.
[28] D. Lin, P. Zhou, W. Fu, Z. Badics, Z. Cendes, A dynamic core loss model for soft ferromagnetic and power ferrite materials in transient finite element analysis, IEEE Trans. Magn. 40 (2) (2004) 1318–1321, https://doi.org/10.1109/TMAG.2004.825025.
[29] E.A. Grunditz, T. Thiringer, Electric vehicle acceleration performance and motor drive cycle energy efficiency trade-off, in: 2018 XIII International Conference on Electrical Machines (ICEM), 2018, pp. 717–723.
[30] E.A. Grunditz, Design and assessment of battery electric vehicle powertrain, with respect to performance, energy consumption and electric motor thermal capability, PhD thesis, 2016.
[31] A. Krings, Iron losses in electrical machines - influence of material properties, manufacturing processes, and inverter operation, Ph.D. thesis, KTH Royal Institute of Technology, 2014, PhD thesis.
[32] T.A. Burress, S.L. Campbell, C. Coomer, C.W. Ayers, A.A. Wereszczak, J.P. Cunningham, L.D. Marlino, L.E. Seiber, H.-T. Lin, Evaluation of the 2010 Toyota Prius hybrid synergy drive system, Tech. rep., ORNL, 3 2011.
[33] C. Kukura, J. Apsley, S. Djurovic, Current-to-flux linkage lookup table design for pm machinery fea-dq hybrid dynamic models, in: 12th International Conference on Power Electronics, Machines and Drives (PEMD 2023), 2023, pp. 72–79.
[34] G. Rang, J. Lim, K. Nam, H.-B. Ihm, H.-G. Kim, A MTPA control scheme for an IPM synchronous motor considering magnet flux variation caused by temperature, in: Nineteenth Annual IEEE Applied Power Electronics Conference and Exposition, 2004, APEC'04, vol. 3, 2004, pp. 1617–1621.
[35] S. Morimoto, M. Sanada, Y. Takeda, Wide-speed operation of interior permanent magnet synchronous motors with high-performance current regulator, IEEE Trans. Ind. Appl. 30 (4) (1994) 920–926, https://doi.org/10.1109/28.297908.
[36] D. Konvicny, P. Makys, M. Furmanik, Effect of increasing the sampling frequency with respect to the bandwidth of the pi controller of current control loop, Transp. Res. Proc. 55 (2021) 935–940, https://doi.org/10.1016/j.trpro.2021.07.190, 14th International scientific conference on sustainable, modern and safe transport.